SUPPLEMENTAL MATERIAL

The Supplemental Material includes sections on (i) details of the LIGASE method for segmentation of neonatal MRI volumes; (ii) registration landmarks for inter-atlas registration; (iii) illustrations of left hemisphere population-average maps of cortical shape for term infants and adults (complementing Fig. 5 of the main Results); (iv) analysis of MRI volumes in the region of the apparent hemispheric depth asymmetry near hippocampal cortex in term infants; (v) sulcal depth values in term infants for the STS local ROI asymmetry analysis; (vi) a comparison of suprathreshold cluster testing and threshold free cluster enhancement.

(i) The LIGASE method. The LIGASE segmentation method includes three main stages: (a) seed-growing, (b) neighbor-refinement, and (c) dilation and manual patching. Key steps in the process are shown in Supplemental Figure 1.

Stages (a) and (b) relied on assigning each voxel initial 'likelihood' values for three tissue types (white matter, gray matter, and CSF) from the histogram of voxel intensities (Suppl-Fig. 2), which typically showed clear peaks but overlapping profiles for each tissue type. This assumes that each tissue profile in the voxel intensity histogram has an asymmetric Gaussian distribution of voxels intensities to assign likelihood values for each tissue type from user estimates for the peak intensity and the width of each profile. Because each profile was asymmetric about its peak, two separates estimates of the width were made, one for the low-intensity and one for the high-intensity side. Specifically, for each profile the user estimated the intensity at 10% of the peak on each side of the distribution. The likelihood value for each tissue type T was calculated according to equation (1):

$$L_T(v) = 0.9e^{C(v-\mu_T)^2/(w_T-\mu_T)^2} \quad (1)$$

where L is the likelihood value, v is the voxel intensity, μ is the estimated profile peak for T, w is the estimated intensity at 10% of the peak for T on either the low (if $v < \mu$) or high (if $v \geq \mu$) intensity side, and C = -2.2 was an empirically determined constant that gave reasonable results.

(a) Seed Growing Stage. The seed growing stage generated an initial white matter segmentation volume from a user-specified seed voxel placed within white matter by iteratively adding adjoining voxels to the segmentation if they were categorized to be in the white matter and halting at the estimated gray/white boundary. The choice of the seed voxel was not critical; in practice it was centered in white matter on an axial slice above the lateral ventricle and below sulcal fundi (Suppl-Fig. 1A black circle).

Starting at the seed voxel, voxels were iteratively tested for inclusion only if they were adjacent (i.e. one of 26 neighbors in 3 dimensions) to a previously segmented voxel. Supplemental Figure 3 schematically shows the seed-growing algorithm. On each iteration, a single voxel, the test voxel, adjacent to a previously segmented reference voxel was evaluated for inclusion in the segmentation. The test voxel was assigned a white matter likelihood value (Equation 1), a pairwise difference (intensity difference between the tested voxel and the previous voxel segmented) and a gradient value (magnitude of a vector whose components are the difference in intensity between adjacent face neighbors of the tested voxel along each axis). The gradient and pairwise difference values served to detect boundaries between tissue classes; high values of the gradient signify the test voxel may be on the edge of a tissue class and high values for the pairwise difference signify the test voxel may be in a different tissue class than the reference voxel. The white matter likelihood value was used to define permissible ranges for the pairwise difference and gradient values. The higher the white matter likelihood the larger the permissible range for the pairwise difference and gradient. Voxels with both the pairwise difference and gradient values within the permissible range were included in the segmentation volume and all adjacent neighbors of the test voxel were included as test voxels in subsequent iterations. The segmentation volume was complete once no additional test voxels were added to the segmentation.

One limitation of the seed growing stage was the difficulty in estimating the width of the white matter profile due to the overlap with the gray matter and CSF profiles. To facilitate selection of near optimal estimates, the user input a range of width estimates spanning the low- and high-intensity sides of the white matter profile. This input range was reduced to a set of evenly spaced values, m_n for the low-intensity estimate and m_x values for the high-intensity estimates. For each possible paring of low-

and high-intensity estimates an independent segmentation volume was generated giving a total of $m_n * m_x$ segmentation volumes. The user examined all segmentation volumes overlaid on the structural MRI and chose the most accurate by visual inspection.

(b) Neighbor Adjustment Stage. Supplemental Figure 1B illustrates a typical output from the seed-growing stage and identifies two common types of errors in the initial segmentation volume. Black circles identify white matter voxels that were not included in the initial segmentation owing to the sensitivity of the gradient and pairwise difference measures to signal inhomogeneity in the white matter and partial volume effects at the gray/white border. The yellow circle identifies a CSF voxels that was included in the segmentation due to partial volume effects at tissue boundaries.

The neighbor adjustment stage improved upon these errors by assigning each voxel initial white matter, gray matter, and CSF likelihood values and iteratively adjusting the white matter likelihood of each voxel based on the likelihood values of its adjacent neighbors. If a voxel was included in the initial segmentation from the seed-growing stage it was automatically assigned a high initial white matter likelihood value (typically 0.85), otherwise its white matter likelihood was calculated as described above. Gray matter and CSF likelihood values were assigned as noted above. During each iteration, a voxel's white matter likelihood was increased for each adjacent voxel with high white matter likelihood and decreased for each adjacent voxels with high gray matter or CSF likelihood. Once a steady state was reached all voxels with a white matter likelihood exceeding a predetermined threshold (typically 0.85) were included in the segmentation.

(c) Dilation and Manual Patching. The segmentation volume from LIGASE was loaded into Caret and dilated by one voxel (1 mm) in all dimensions to achieve a boundary that approximates the cortical mid-thickness (cortical layer 4, Suppl.-Fig. 1D). Neonatal cortex is approximately 2 mm thick in most regions (Bayer and Altman, 2003); at a resolution of 1x1x1 mm the neonate cortex typically includes one clear gray matter voxel bounded by one voxel overlapping with white matter voxel and one voxel overlapping with CSF. The dilation placed the boundary of the segmentation at the outer edge of the clear gray matter voxel

In general each hemisphere contains some segmentation errors that required manual editing using volume editing tools in Caret (Suppl.-Fig. 1D, black circle). This was especially common in medial temporal regions where the transition to hippocampal cortex and amygdala is often difficult to determine with an automated algorithm. The fundus of the parahippocampal sulcus and the anterior extent of the hippocampus were delineated with the aid of a photographic atlas of neonatal neuroanatomy (Bayer and Altman, 2003). Supplemental Figure 1E shows a slice through a final segmentation volume.

(ii) Inter-atlas registration. Supplemental Figure 4 shows the 22 landmarks used for inter-atlas registration displayed on the PALS-term12 (top) and PALS-B12 (bottom) average inflated surfaces. These landmarks include the average 'Core-Six' plus 16 other landmarks readily identifiable on each hemisphere's average surface. The 16 additional landmarks were drawn independently on the age-specific average right hemisphere fiducial surface. Age-specific maps of population average curvature assisted in drawing landmarks along average sulcal fundi. The termination points for these landmarks were chosen to maintain similar relative distances to other registration landmarks or surface feature for each age group.

(iii) Left Hemisphere Population Average Maps. Supplemental Figure 5 shows population average maps of cortical structure for the left hemisphere for both term infant and adult population. Maps of average cortical shape and sulcal depth for each population are shown for lateral (Suppl.-Fig. 5A, top) and medial (Suppl.-Fig. 5A, bottom) surface views. As was evident for the right hemisphere (see main text) this side-by-side comparison demonstrates broad similarities between term infants (Suppl.-Fig. 5A, rows 1, 3**)** and adults (Suppl.-Fig. 5A, rows 2, 4). The average fiducial and average sulcal depth maps indicate that adult sulci are deeper by up to 10 mm, but the same overall shape (sulci and gyri in the average fiducial surfaces, dark and bright areas on the average sulcal depth map) is evident at both ages. Supplemental Figure 5B shows maps of inter-individual variability in both sulcal depth (sulcal depth variability) and spatial position (3D coordinate variability) for each age group. These maps are shown for lateral

(Suppl.-Fig. 5B, top) and medial (Suppl.-Fig. 5B, bottom) views for both infants (Suppl.-Fig. 5B, rows 1, 3) and adults (Suppl.-Fig. 5B, rows 2, 4). As these surfaces were normalized for overall cortical dimensions, the variability in each measure was minimally affected by differences in total brain dimensions. The pattern of variability is heterogeneous at each age, indicating that some regions of the cortex (blue/green) are more consistent in shape than others (orange/red). Importantly, the adult and term infant patterns of variability are quite similar overall, suggesting that this pattern is established by term birth and changes only modestly by adulthood.

(iv) Apparent term infant hemispheric depth asymmetry. In the main results an apparent right-deeper-than-left hemispheric depth asymmetry was detected along the parahippocampal sulcus and non-cortical medial wall in term infants. As this asymmetry lies in a region where delineating the limit of neocortex in the hippocampal fissure is difficult using MRI data we investigated the biological significance of this asymmetry by analyzing MRI volumes of individual term infants. The top half of Supplemental Figure 6 shows the apparent depth asymmetry (Suppl.-Fig. 6A, red region) and an example of a term infant coronal MRI slice that intersects the apparent asymmetry (Suppl.-Fig. 6B). Supplemental Figure 6C shows coronal MRI slices for 3 term infants. For each infant, three coronal MRI slices are shown that intersect the apparent asymmetry along its anterior (slice A), middle (slice B), and posterior (slice C) extent. The approximate locations of these slices relative to the apparent depth asymmetry are noted by arrows in Supplemental Figure 6A. The MRI volumes have been cropped along the red box indicated in Supplemental Figure 6B. Surface contours illustrating the intersection of each individual's left (red contour) and right (blue contour) fiducial surfaces with the MRI volume are overlaid on each volume. The upper left panel (term 2, slice A) identifies the portion of the contour lying within the apparent depth asymmetry (black circles).

For all slices of each infant the right contour follows the fundus of the parahippocampal sulcus more closely on the MRI volume than the left contour. This discrepancy results in the right contours extending deeper into the parahippocampal sulcus than the left, which accounts for the apparent depth asymmetry. Accordingly we

do not consider this asymmetry to be biologically significant.

(v) STS local ROI asymmetry analysis for term infants. A significant depth difference along the STS was not detected in term infants by TFCE analysis (see main text). However, the depth difference map in the term infant population indicates that the STS is deeper on the right over much of its extent (see main text Fig. 6). We therefore used a more sensitive method that is less affected by variability in sulcal trajectory and imperfections in the registration algorithm. We traced the sulcal fundus of each individual and tested for significant depth asymmetry within a narrow region of interest (ROI) along the middle portion of the STS in term infants, which corresponds to the region of significant asymmetry in adults. Supplemental Table 1 lists the mean sulcal depth (in mm) within the ROI for the left hemisphere (column 2), right hemisphere (column 3), and the mean depth difference between hemispheres (columne 4) for each term infant. Population average values are listed at the bottom. By this analysis the central portion of the STS fundus was 1.7 mm deeper on average on the right than the left ($t=5.2$, $p<0.01$).

(vi) Comparison of suprathreshold cluster testing and threshold free cluster enhancement. Supplemental Figure 7A shows a t-map (left) of hemispheric sulcal depth difference in adults and several maps (right) showing the results of significance testing using a suprathreshold cluster test (Nichols and Holmes, 2002; Van Essen et al., 2006). For each test, significance was determined using a different initial cluster-forming threshold and 2500 iterations of permutation. The t-value corresponding to the initial cluster-forming threshold is listed next to each map. Nodes that passed significance are colored according to laterality: deeper on the right (red) and deeper on the left (blue). As expected, decreasing the threshold emphasizes clusters with low t-values and large spatial extent but at the expense of smaller clusters with higher t-values. The bottom half of the figure (Suppl.-Fig. 7B, C) shows TFCE maps (left) and the location of nodes that passed significance by TFCE testing (right) for two values of E in the TFCE transform (see main Methods Eq. 1). Each map was generated using an H value of 2.0 and an E value of 1.0 (Suppl.-Fig. 7B) or 0.5 (Suppl.-Fig. 7C). Comparing the results of the suprathreshold

cluster and TFCE testing reveals that TFCE is sensitive to both t-value and spatial extent. In particular, in the TFCE test the cluster lying along the superior temporal sulcus (Suppl-Fig. 7B, red cluster) passed significance due to the large spatial extent of the supporting section for that cluster whereas the cluster lying along the Sylvian fissure (Suppl-Fig. 7B, blue cluster) passed significance due to its large t-value. Additionally, while extent of the significant regions was larger using E=1.0, the location of the regions remained the same.

Supplemental Figure Legends

Supplemental Figure 1. Key steps in the LIGASE segmentation method. Segmentation volumes are shown in red and overlaid on a right hemisphere T2-weighted coronal MRI slice of a term infant. (A) Location of the user-specified seed voxel (black circle) for the seed-growing stage. (B) Initial white matter segmentation output from the seed growing stage. White matter voxels not included (black circles) and CSF voxels that were included (yellow circle) are identified. (C) Revised white matter segmentation output from the neighbor adjustment stage. (D) Mid-cortical segmentation volume achieved by 1-voxel dilation of the output volume from the neighbor adjustment stage. The black circle identifies a region where the dilation caused two gyri to join. (E) Final segmentation output after manual patching. The non-cortical medial wall from the fundus of the parahippocampal sulcus inferiorly to the callosal sulcus superiorly has been manually delineated and smoothed.

Supplemental Figure 2. Histogram of voxel intensities for a right hemisphere T2-weighted coronal MRI slice of a term infant. Voxel values have been scaled to a range of 0 to 255. The histogram shows clear peaks but overlapping profiles for gray matter, white matter, and CSF voxels. GM, gray matter profile; WM, white matter profile; CSF, cerebral spinal fluid profile

Supplemental Figure 3. Schematic outline of the algorithm for the seed-growing stage of the LIGASE method. See supplemental text for details. WM, white matter.

Supplemental Figure 4. Inter-atlas registration landmarks used to register the PALSB-12 atlas to the PALS-term12 atlas. Landmarks are displayed on the average PALS-term12 (top) and average PALS-B12 inflated surfaces. Surfaces have been colored according population-average sulcal depth for each age group. CaS, calcarine sulcus; CeS, central sulcus; CiS, cingulate sulcus; IFS, inferior frontal sulcus; pIPS, posterior portion of the intraparietal sulcus; ITS, inferior temporal sulcus; dMW, dorsal portion of the medial wall; vMW, ventral portion of the medial wall; CoS, collateral sulcus; MTS,

medial temporal sulcus; OlS, olfactory sulcus; OrS, orbital sulcus; POS, parietal-occipital sulcus; PoCeS, postcentral sulcus; PreCunS, precuneus sulcus; sPreCeS, superior portion of the precentral sulcus; SFS, superior frontal sulcus; STG, superior temporal gyrus; STS, superior temporal sulcus; iPreCeS, inferior portion of the precentral sulcus; SF, Sylvian fissure; aIPS, anterior portion of the intraparietal sulcus.

Supplemental Figure 5. Left hemisphere population averaged maps for the term infant and adult populations. Rows 1 and 2 show lateral views for a population of 12 term infants and 12 adults, respectively. Rows 3 and 4 show corresponding medial views for term infants and adults, respectively. All maps were generated after surface based scale normalization. (A) Average fiducial and average sulcal depth maps. The average fiducial surface was created by calculating the average spatial coordinate from all 12 individuals after surface-based scale normalization. The average sulcal depth maps were created by calculating the average sulcal depth across individuals for each node. Note scale differences for each age group. (B) Maps of sulcal depth and 3D positional variability displayed on the standard mesh average term infant inflated surface. Sulcal depth variability maps display the standard deviation in sulcal depth for all individuals. 3D positional variability maps display the standard deviation in 3D fiducial coordinate position for all individuals. Note scale differences for each age group. Average sulcal depth variability and 3D positional variability maps for the term infants and adults are displayed on the PALS-term12 and PALS-B12 standard mesh average inflated surfaces, respectively.

Supplemental Figure 6. Examination of apparent depth asymmetry along the fundus of the parahippocampal sulcus in term infants. (A) Medial view of the term infant average inflated surface displaying the location of the apparent depth asymmetry (red region). The letters correspond to slice locations shown in (C). (B) Example term infant coronal MRI that intersects the apparent depth asymmetry at the level of slice B. The red box indicates the approximate cropped region displayed in (C). (C). Cropped coronal MRI volumes for 3 term infants in the vicinity of the parahippocampal sulcus. For each infant, three coronal MRI slices are shown that intersect the apparent asymmetry along its

anterior (slice A), middle (slice B), and posterior (slice C) extent. Surface contours illustrating the intersection of each individual's left (red contour) and right (blue contour) fiducial surfaces with the MRI volume are overlaid on each volume. The upper left panel identifies the portion of the contour lying within the apparent depth asymmetry (black circles).

Supplemental Table 1. Examination of sulcal depth asymmetry within an ROI running along the middle extent of the fundus of the superior temporal sulcus in term infants. Mean sulcal depth for each hemisphere and hemispheric depth difference (in mm) within the ROI is given for each term infant. The bottom row lists the mean depth for each hemisphere and mean depth difference. Significance testing was done using a paired t-test.

Supplemental Figure 7. Comparison of suprathreshold cluster testing and threshold free cluster enhancement. (A) Non-thresholded paired t-statistic map for hemispheric depth difference (left) in term infants and the locations of clusters that passed significance testing using a suprathresold cluster test (right). The t-value corresponding to the initial cluster forming threshold is listed next to each map. (B) TFCE-statistic map (left) generated by applying a TFCE transform with H value of 2 and E value of 1 to the t-statistic at each surface node and the location of significant depth difference clusters revealed by TFCE and permutation testing (right). (C) TFCE-statistic map (left) generated by applying a TFCE transform with H value of 2 and E value of 0.5 to the t-statistic at each surface node and the location of significant depth difference clusters revealed by TFCE and permutation testing (right). For all maps blue clusters are deeper on the left and red clusters are deeper on the right.

Supplemental Figures

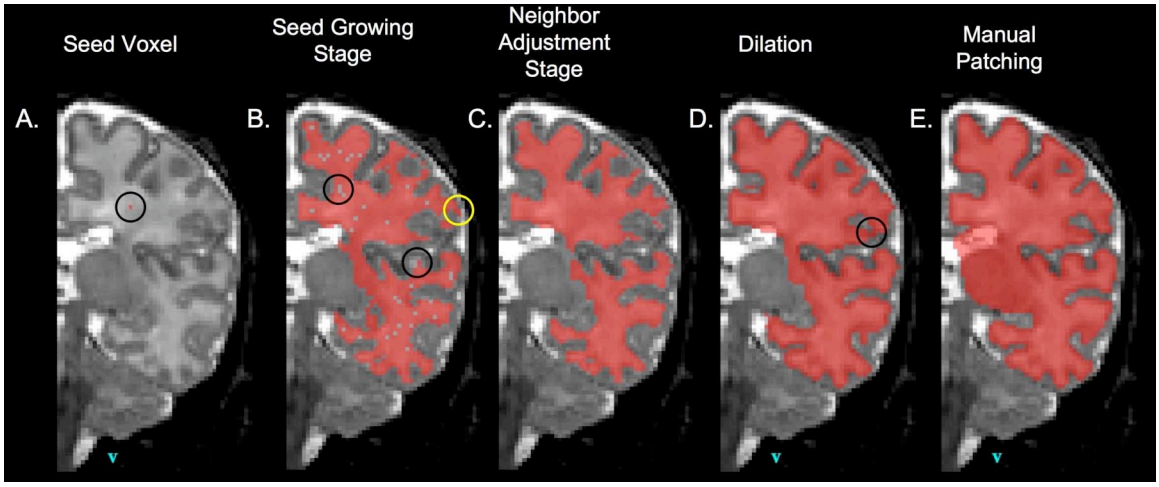

Supplemental Figure 1.

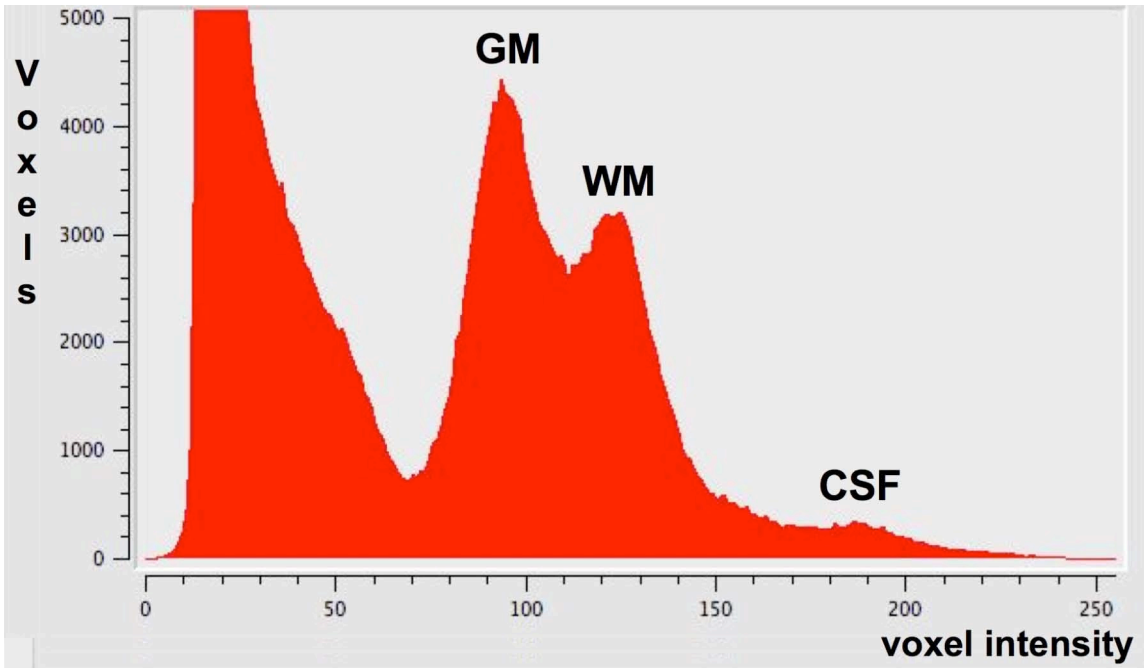

Supplemental Figure 2.

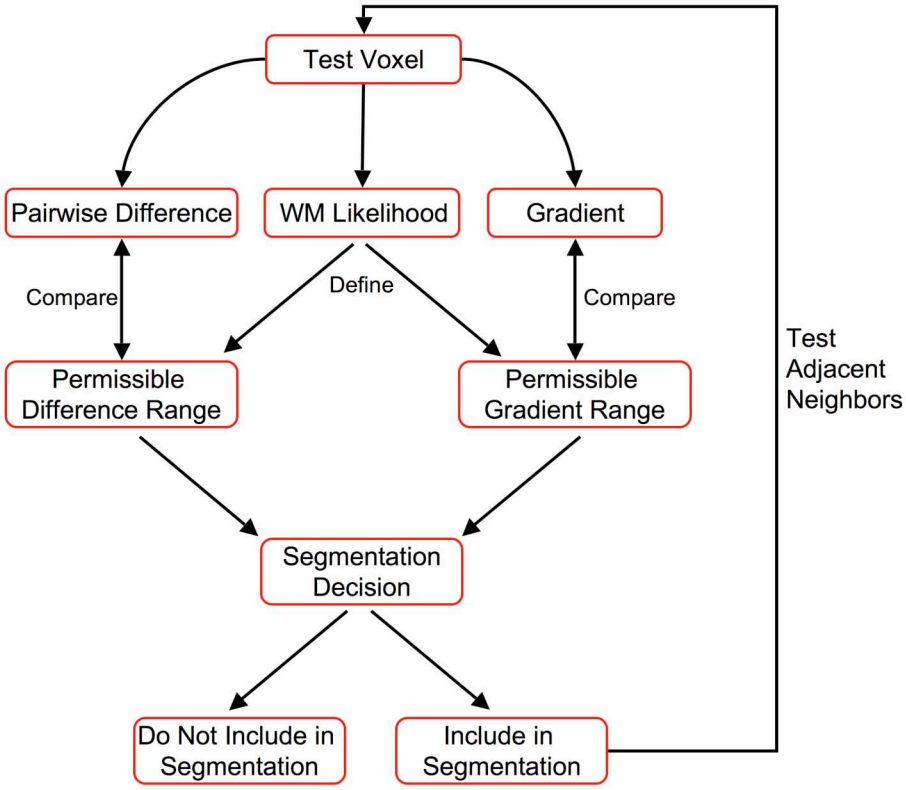

Supplemental Figure 3.

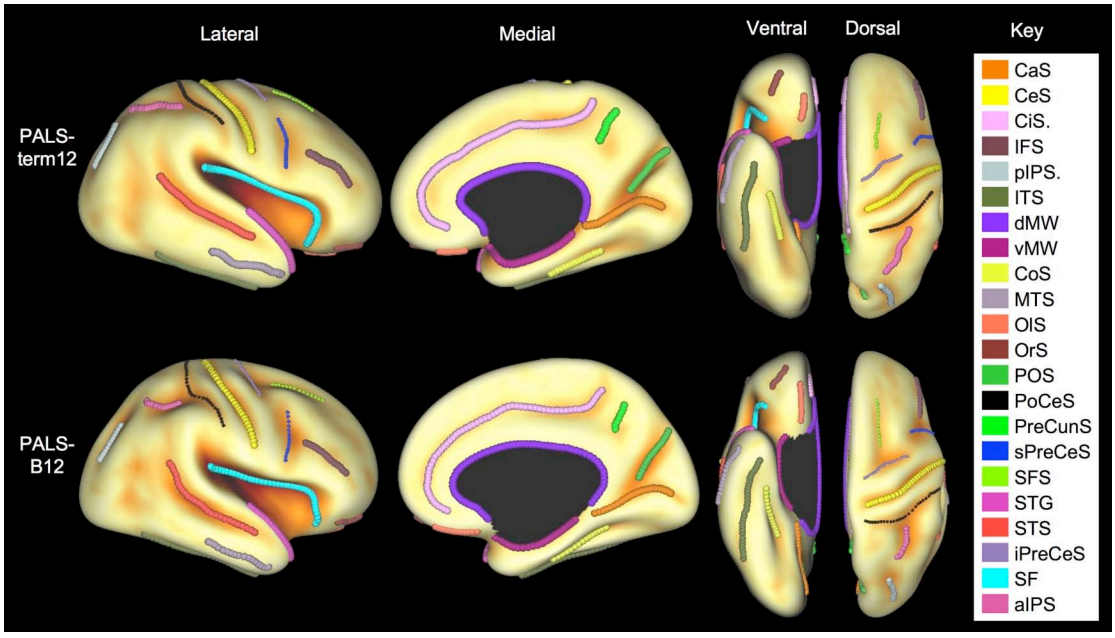

Supplemental Figure 4.

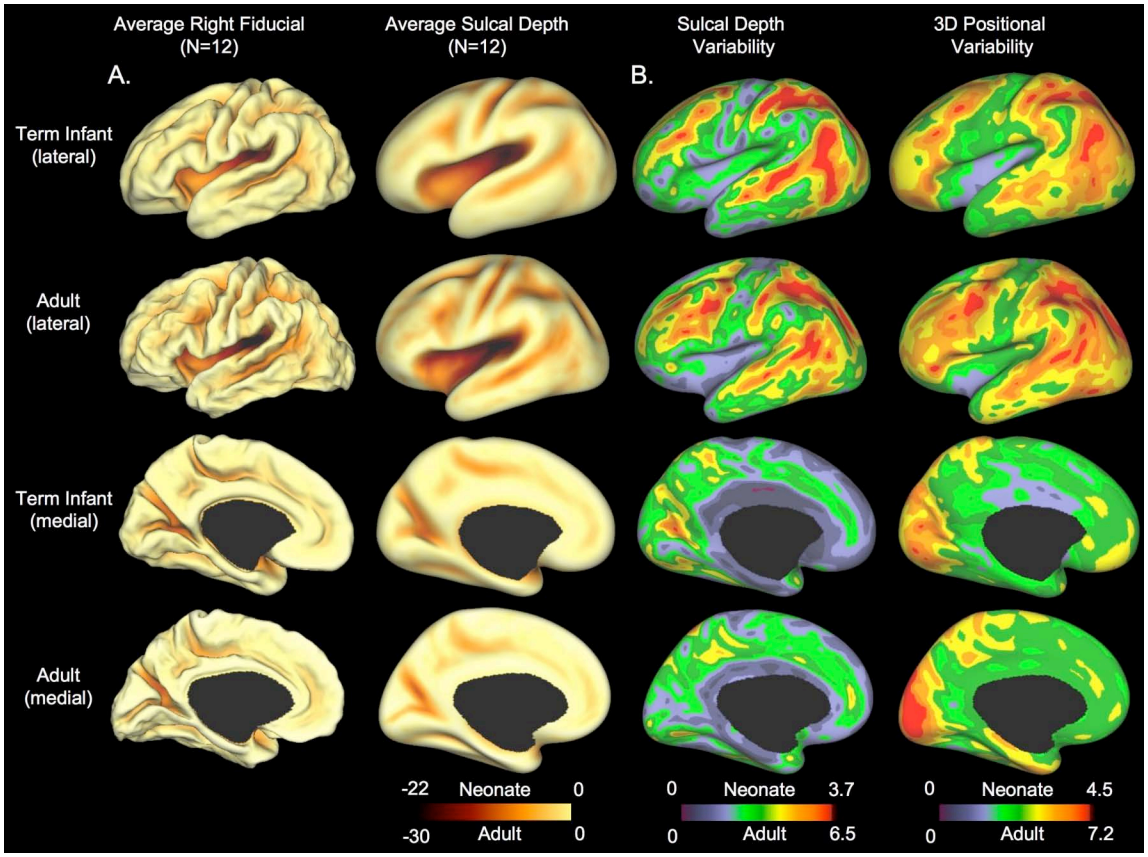

Supplemental Figure 5.

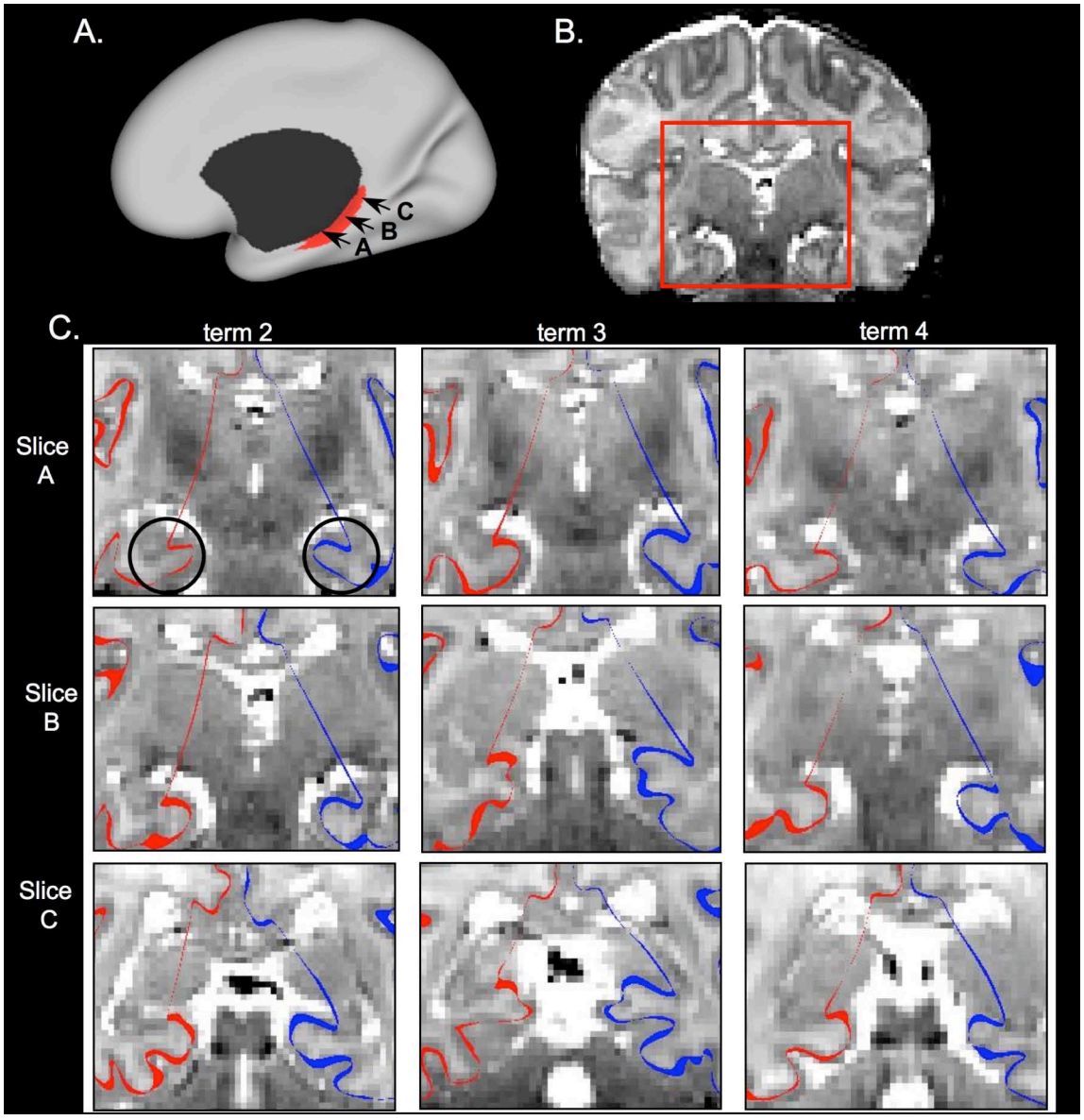

Supplemental Figure 6.

Supplemental Table 1
Term Infant STS ROI Depth Asymmetry

	ROI Mean Depth (mm)			
Subject	Left Hemisphere	Right Hemisphere	Depth Difference (mm)	Paired p-value
Term 1	6.5	9.5	3.0	**<0.001**
Term 2	8.9	11.2	2.3	
Term 3	11.5	11.3	0.2	
Term 4	7.3	9.5	2.2	
Term 5	7.7	10.2	2.5	
Term 6	10.0	11.4	1.4	
Term 7	10.0	11.6	1.6	
Term 8	7.2	10.2	3.0	
Term 9	7.6	10.1	2.5	
Term 10	8.2	8.4	0.2	
Term 11	9.1	10.1	1.0	
Term 12	8.4	9.1	0.7	
Population Mean	8.5	10.2	1.7	

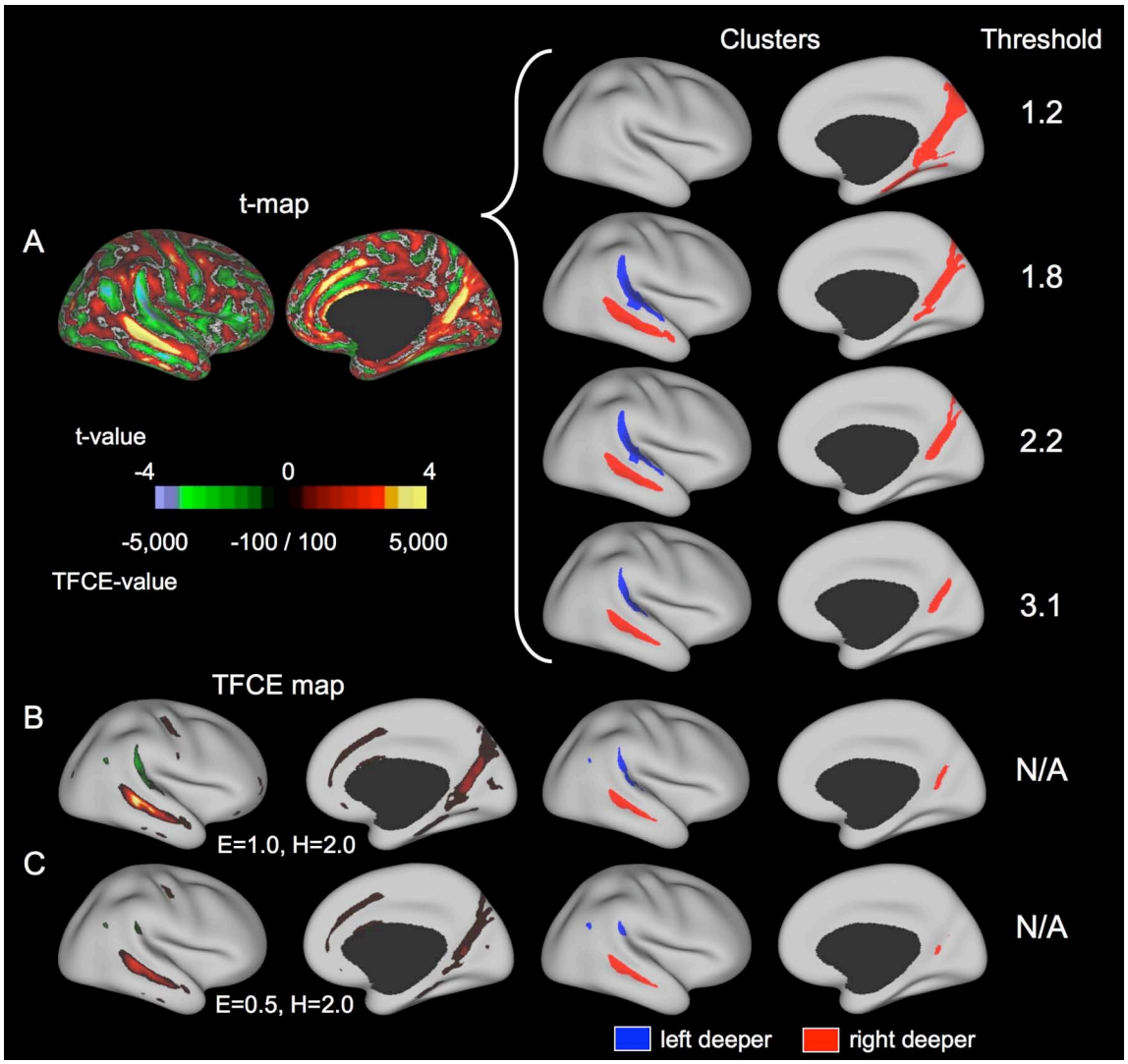

Supplemental Figure 7.

References

Bayer SA, Altman J (2003) The Human Brain During the Third Trimester CRC Press.

Nichols TE, Holmes AP (2002) Nonparametric permutation tests for functional neuroimaging: a primer with examples. Hum Brain Mapp 15:1-25.

Van Essen DC, Dierker D, Snyder AZ, Raichle ME, Reiss AL, Korenberg J (2006) Symmetry of cortical folding abnormalities in Williams syndrome revealed by surface-based analyses. J Neurosci 26:5470-5483.